atmosphere

MDPI

Article

Temperature Retrievals for a Three-Channel Rayleigh Lidar System

Satyaki Das [1,2,*], Richard Collins [1,2,*] and Jintai Li [1]

[1] Geophysical Institute, University of Alaska Fairbanks, Fairbanks, AK 99775, USA; jli23@alaska.edu
[2] Department of Atmospheric Sciences, University of Alaska Fairbanks, Fairbanks, AK 99775, USA
* Correspondence: sdas8@alaska.edu (S.D.); rlcollins@alaska.edu (R.C.)

Abstract

We present the performance of a middle atmosphere Rayleigh lidar system that employs three receiver channels. We characterize the biases in the density and temperature profiles retrieved from each of the receiver channels as well as the combined receiver signal. We associate these biases with pulse pile-up, gain switching, and variations in the detector gain due to signal amplitude. We use a top-down temperature convergence methodology to determine the upper altitude up to which the signals should be compensated for the variations in detector gain. We find that the channels have warm biases in their temperatures of 2–8 K at 40 km. These biases decrease to between 1 K and 3 K at 60 km. Uncertainty estimates derived from the photon-counting statistics indicate temperature uncertainties on the order of 2–5 K in the 40–70 km region, which are consistent with the observed level of inter-channel variability after correction. A comparison with MERRA-2 reanalysis indicates an overall agreement in temperatures and differences that are consistent with the comparisons between the Rayleigh lidars and MERRA-02 at other sites. These results demonstrate that the proposed approach proves reliable for processing the multi-channel Rayleigh lidar data, particularly for systems employing more than two detection channels, and improves the fidelity and accuracy of the temperature retrievals.

Keywords: middle atmosphere; Rayleigh density and temperature lidar; multi-channel lidar; instrumental biases

1. Introduction

Prompted by the need to understand the climate change that is observed in the stratosphere, Rayleigh lidars have proven a critical research tool for studies of the weather and climate of the middle atmosphere [1]. Specifically, these lidar systems have yielded long-term stable measurements of the stratospheric–mesospheric temperature profile. Analysis of these data has revealed long-term trends in the middle atmosphere [2–8]. These trends consistently show that the middle atmosphere is cooling. However, there is significant variability between the amplitude of the cooling trends reported from different sites, and this has been attributed to geographic variation, differences in retrieval algorithms, or some combination of both [9].

The success of Rayleigh lidars has been based on the relative simplicity of the technique. The measurements can be made with broadband light sources (initially high-altitude search lights and later commercial solid-state lasers) and standard photodetectors (cameras and later photomultiplier tubes). The lidar echo is proportional to the atmospheric density, and with an assumption of hydrostatic equilibrium, the temperature profile can be derived from

Academic Editor: Stephan Havemann

Received: 27 February 2026
Revised: 8 April 2026
Accepted: 13 April 2026
Published: 15 April 2026

the lidar signal. The modern Rayleigh lidars followed a generation of instruments based on high-altitude searchlights that yielded temperature profiles of over 65 km by the early 1950s [10–12]. The initial lidars were based on solid-state ruby lasers [13–15]. The modern lidars based on Neodymium Yttrium-Aluminum Garnet (Nd:YAG) lasers, due to their superior performance in terms of optical power and operational stability, were deployed in the 1970s [16–18]. Since then, Nd:YAG lasers have become the prevailing transmitter employed in the Rayleigh lidar systems [19–25].

From the earliest observations, the challenges in acquiring laser echoes from the atmosphere that were proportional to the atmospheric density profile from altitudes of ~30 to 90 km (the fidelity of the lidar signal) were recognized [13,15]. Several research groups have presented in-depth analyses of the performance and fidelity of their Rayleigh lidar systems [26–28]. However, even in the presentations by the Network for the Detection of Atmospheric Composition Change (NDAAC), it is more common for authors to present a summary analysis without presenting any raw lidar signals, citing, for example: "The high and low-gain Rayleigh channels are electronically gated. . ." [24].

In this paper, we present an analysis of a three-channel Rayleigh lidar system. We consider the fidelity of the lidar signals in all three channels, correcting them for pulse pile-up, electronic gating, and finally for signal amplitude. The three channels are then combined to yield one high-amplitude lidar signal profile that is used to yield a single temperature profile. We present the performance of the lidar in terms of incremental changes in temperature as the corrections are made to the signal, and in terms of the combined lidar signal profile and the derived density and temperature profiles.

2. Instrument

The Rayleigh Density Temperature Lidar system (RDTL) at the Lidar Research Laboratory (LRL), Poker Flat Research Range (PFRR), Chatanika, Alaska (65° N, 213° E), is based on a Rayleigh lidar that was originally deployed in Alaska in November 1997. The lidar was initially developed as part of the "Alaska Project", which was a collaboration between the National Institute of Information and Communications Technology (NICT), Tokyo and the Geophysical Institute of the University of Alaska, Fairbanks, Alaska (GI-UAF) [29]. The RDTL lidar, which initially had a one-channel receiver system [30] was modified to a two-channel system in 2015 [31] and a three-channel system in 2017 [32]. The three-channel system enables the use of a larger telescope aperture, allowing for increased signal collection while preventing saturation of the photomultiplier tubes (PMTs). This results in an improved signal-to-noise ratio (SNR), particularly at higher altitudes, and reduces the uncertainties in the retrieved temperature profiles, thereby enabling high-resolution measurements of atmospheric wave structures. Compared to a conventional two-channel lidar system, the three-channel configuration provides improved handling of the large dynamic range of atmospheric backscatter signals by distributing the signal across three distinct intensity regimes. This reduces the saturation effects at lower altitudes while enhancing the sensitivity at higher altitudes, leading to more accurate and robust temperature retrievals.

Comparative studies have been presented showing the consistency between the temperatures measured by the Rayleigh lidar and the sounding of the Atmosphere using a Broadband Emission Radiometry (SABER) instrument aboard the Thermosphere–Ionosphere–Mesosphere Energetics and Dynamics (TIMED) satellite and the Fourier Transform Spectrometer aboard the Atmospheric Chemistry Experiment satellite [33,34].

A schematic diagram of the RDTL is presented in Figure 1, and the system specifications are listed in Table 1. The system employs a 1.04 m Cassegrain telescope and a Nd:YAG laser operating at 532 nm, 20 pulses-per-second (pps), with an average power of 9–10 W. The laser beam is directed through a beam expander (BE) with a magnification

of 10. The beam is directed into the sky by a beam steering mirror (BSM) at 45°. A fast photodiode (PD) detects the laser pulse. The RDTL receiver system is then divided into three identical channels that each include a beam splitter (BS, Channel 1 and 2) or a mirror (Channel 3), an interference filter (IF) of bandwidth (0.3 nm, FWHM), a focusing lens (FL), a photomultiplier tube (PMT), a pre-amplifier (PA), a delay generator (DG), a multi-channel scaler (MCS) and a computer. The three IFs are each housed in an oven that maintains their temperatures at 25 °C and avoids thermally induced drifts in their center wavelengths and transmission. The MCS units operate in a photon counting mode and count the amplified PMT pulses (or photon counts) in 4096 consecutive 320 ns (48 m) intervals. This yields a raw signal that extends from a range of 0 to 196.6 km at 48 m resolution. The laser Q-switch triggers the DG, while the PD triggers the MCS. Thus, the PMT is gain-switched prior to the laser firing. This provides a margin of protection for the PMT. The RDTL is biaxial. The laser beam exits the LRL-PFRR six meters (6 m) from the center of the receiver telescope. Thus, the receiver and the laser beam overlap at ~12 km (1 mrad field-of-view (FOV)) or at ~6 km (2 mrad FOV). The overlap function serves to further protect the receiver PMTs from the large amplitude signals and from the lower troposphere. The laser operates in a free-running mode, triggered by its internal control system. The lidar system receiver is synchronized to the laser.

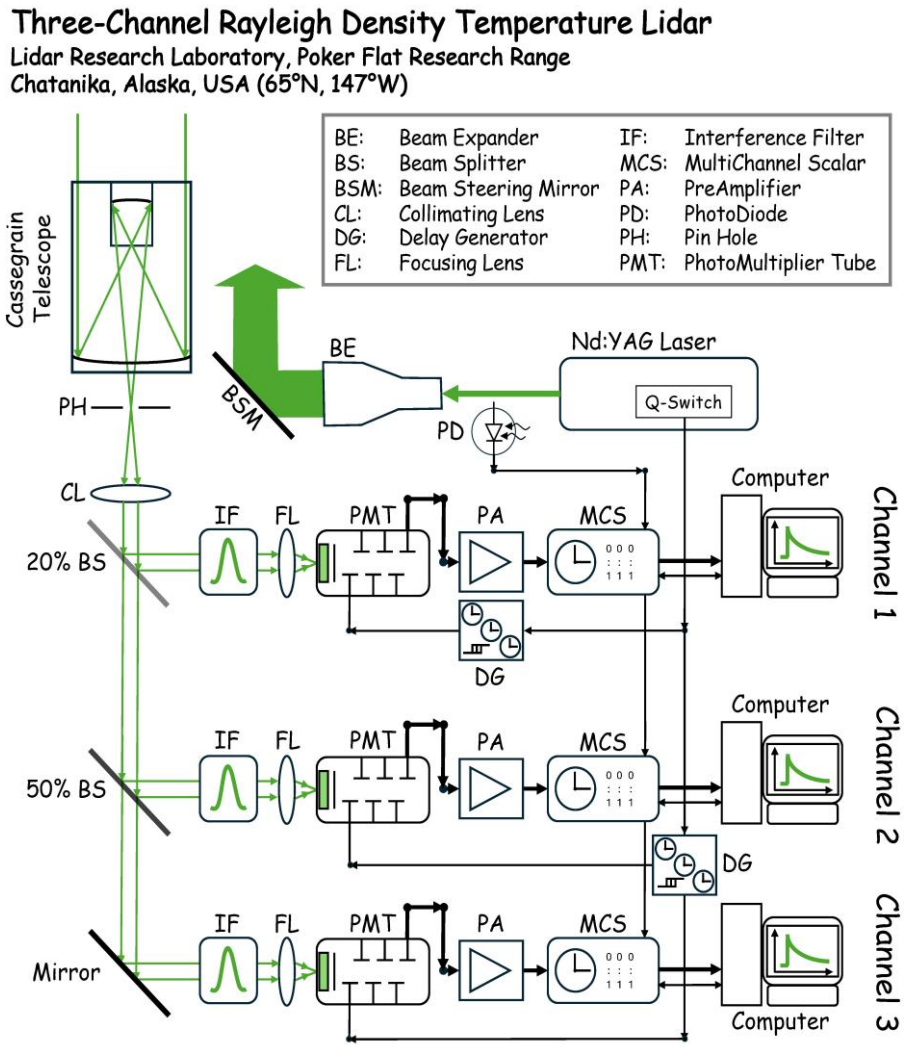

Figure 1. A schematic diagram of the three-channel Rayleigh Density Temperature Lidar system installed at the Lidar Research Laboratory, Poker Flat Research Range, Chatanika, Alaska.

Table 1. RDTL specifications.

Specification	Description
Transmitter	
Laser	Nd:YAG
Model	Continuum Powerlite 8020
Wavelength (λ_L)	532 nm
Repetition rate (R_L)	20 Hz
Pulse energy (E_L)	450–500 mJ
Pulse width	5–7 ns
Divergence	0.45 mrad
Beam expander	×10
Receiver	
Telescope diameter	1.04 m
Field of view	1.0 mrad FWHM
Interference bandwidth	0.3 nm
Preamplifier	Stanford Research Systems SR445
Preamplifier gain/bandwidth	5/300 MHz
PhotoMultiplier tube	Hamamatsu RS3234-1
PhotoMultiplier socket	Hamamatsu C1392-51 MOD
Multi-Channel scaler	Stanford Research Systems SR430
Maximum MCS count rate	100 MHz
Detector dead time	8 ns
Range resolution	320 ns/48 m

The telescope is a 1.04 m Cassegrain Telescope with a f-number of f/15. This slow telescope was originally designed for planetary viewing. With a focal length of 15.6 m, the telescope has an image size of 15.6 mm for a 1 mrad FWHM FOV. With this large image, the receiver is free-space-coupled rather than fiber-coupled. To avoid an overloading of the photomultiplier tubes, the tubes were gain-switched by reverse biasing the first dynode with 200 V for a specified length of time after the laser Q-switch fires. This switching is implemented through a specialized PMT socket that provides two inputs, timing and bias voltage, to control the first anode of the PMT. In Channel 1, the PMT switching is controlled by the DG with a delay of 150 µs. In channels 2 and 3, the PMT switching is controlled by the DG with a delay of 200 µs. The PMTs are biased at −2000 V with independent power supplies. Channel 1 receives about 20% of the total received optical signal, while Channel 2 receives about 40% (50% of 80%), and Channel 3 receives about 40% (100% of 40%). The lidar receiver performs as a non-paralyzable system with a deadtime of 8 ns based on a system analysis of photon counting and pulse pile-up [35,36].

The data acquisition of the lidar signal is controlled by the operator using the computer in the MCS unit. The data acquisition is organized as follows. A raw laser profile is acquired by the MCS unit by integrating the echoes from a given number of laser pulses (typically 1000). Once a laser profile is acquired, the data is transferred from the MCS buffer to the computer. A sequence of laser profiles (typically 16) called a set is acquired and saved to a single ASCII file on the computer. Once a set is complete, the operator initiates the next set. Each set of 16 1000-pulse profiles takes about 800 s to acquire (there is a small variation of less than 10 s due to the communication and data transfer times between the computer and the MCS). In a 12 h observation period, there are typically 50 sets of data acquired. This approach, where the operator prompts the acquisition as a sequence of sets, provides for a regular pause in the data acquisition to allow the operator to adjust the system as required (e.g., optimize the alignment of the transmitter and receiver and adjust the second harmonic generator in the laser to maximize laser energy). At the beginning

of every observation, the alignment of the transmitter and receiver is optimized based on maximizing the lidar signal from a high altitude (typically 60–65 km).

3. The RDTL Signals

In this study, we illustrate the performance of the RDTL with a set of observations made on the night of 18–19 October 2018. Figure 2 shows the lidar signal profile for the three-channel Rayleigh lidar system acquired between 1826 and 0604 LST (0326 and 1504, 19 October 2018, UT). This represents the total raw lidar signal acquired over 11.3 h from 816,000 laser pulses. The data was acquired as a series of 816 profiles of 1000 pulses. These 816 profiles were acquired as 51 sets of 16 profiles each. Thus, the data is annotated as extending from set 1, profile 1 (i.e., 1/1) to set 51, profile 16 (i.e., 54/16). The lower horizontal axis shows the total lidar signal, while the upper horizontal axis shows the count rate. The lidar signals are summarized in Table 2. Of immediate import is the fact that the signal count rates are less than 10 MHz, indicating that a pulse pile-up is not a major source of distortion that reduces the fidelity of the lidar signal, as the receiver has a maximum count rate of 100 MHz and the PMT and PA bandwidths are 200 MHz and 300 MHz, respectively. We note the count rates above 120 km are 63/68/110 counts per second for channels 1, 2, and 3, respectively. For the RDTL PMTs, the expected dark counts are 8–55 counts per second, so the background signals are within the variability of the dark count signals [32].

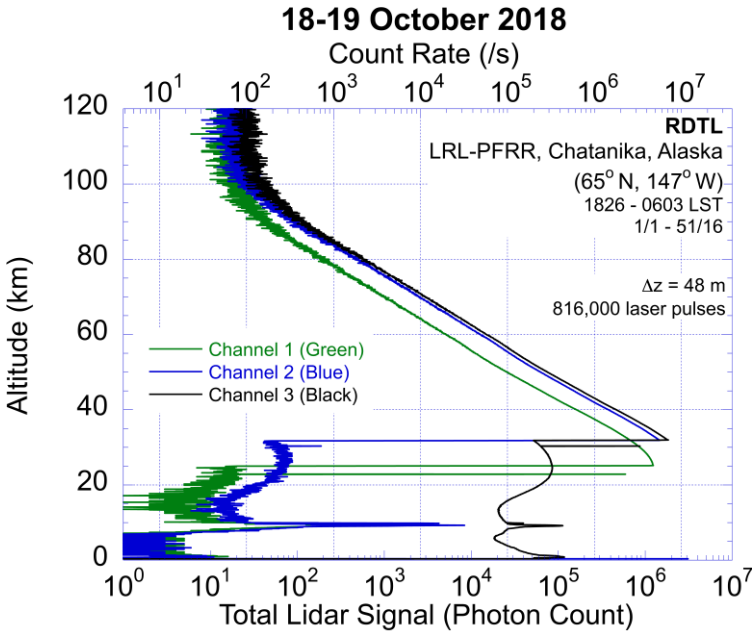

Figure 2. The PFRR-RDTL total lidar signal and signal count rate plotted as a function of altitude on 18–19 October 2018. The grids are associated with the count rates and not the lidar signal.

The total lidar signal (N_{TOT}) is composed of three components: atmospheric signal (N_S), background signal, and dark signal. This signal decomposition is a well-established statistical method [37]. The associated uncertainties in the signals are described by Poisson statistics [38]. At altitudes above the gain switching, the background and dark signals are constant with the altitude and may be estimated as the average of the signal between 190 km and 195 km. Thus, the atmospheric signal is estimated by the subtraction of this constant signal from the total signal. The uncertainty in the signal is effectively given by the square root of the total lidar signal. The signals and errors are presented in Table 2. We first see that Channel 1, Channel 2, and Channel 3 signals represent 16%, 39%, and 45%

of the acquired three-channel lidar signals. The difference in the proportions of the lidar signals (nominally 20%, 40%, and 40%) reflects the variations in the IF transmission in each channel. The relative uncertainties in the three-channel signals increase in altitude from 0.03/0.02/0.02% at 42.5 km to 0.2/0.1/0.1% at 62.5 km and 1/0.6/0.5% at 82.5 km.

Table 2. A summary of the PFRR-RDTL signals on the night of 18–19 October 2018.

Altitude (km)	Number of Range Bins	N_{TOT} (Photon Count)	N_S (Photon Count)	ΔN_S (Photon Count)
		Channel 1/2/3	Channel 1/2/3	Channel 1/2/3
42.5 (40–45)	104	1.08/2.55/ 3.12×10^7	1.08/2.53/ 3.12×10^7	3.28/5.03/ 5.58×10^3
62.5 (60–65)	104	3.67/9.17/ 10.8×10^5	3.65/9.15/ 10.7×10^5	6.04/9.56/ 10.3×10^2
82.5 (80–85)	105	1.42/3.42/ 4.06×10^4	1.24/3.23/ 3.77×10^4	1.11/1.79/ 1.94×10^2
122.5 (120–125)	104	1.69/1.84/ 2.89×10^3	−1.8/0.3/ 4.6×10^1	n/a/1.73/ 6.70×10^0
192.5 (190–195)	104	1.71/1.84/ 2.84×10^3	0/0/0	0/0/0

4. Rayleigh Lidar Density and Temperature Retrievals

4.1. Uncorrected Raw Lidar Signals

The raw photon count profiles are combined in time and altitude, the background is subtracted, and the raw photon counts are corrected for range scaling and extinction. We follow established methods, calculate the combined background and average dark photon count signal at 190–195 km and correct the lidar signals for extinction [39]. The corrected atmospheric lidar signal is used to estimate the density profile using standard lidar inversion techniques, where the lidar signal is range-corrected (e.g., [16,30,40]). The density profile is smoothed by 2 km (i.e., 41 range bins) and normalized to yield a normalized density profile [41]. The ratio of the Channel 2 density to the Channel 1 density increases with increasing altitude. When normalizing the ratio to 1 at 85 km, the ratio increases from 0.87 at 40 km. Similarly, the ratio of the Channel 3 density to the Channel 1 density increases with increasing altitude from 0.93 at 40 km to 1 at 85 km.

The retrieval of the atmospheric temperature profile from the atmospheric density profile follows the established hydrostatic method (e.g., [16]). The retrieval with an estimate of the acceleration due to gravity at Chatanika of 9.8228 m s^{-2} [33]. The method assumes that there is a negligible contribution to the lidar signal from aerosols, polar stratospheric clouds, or noctilucent clouds (e.g., [42–44]). The method also requires an estimate of the temperature at 85 km that is taken from the Stratospheric Processes and their Role in Climate (SPARC) [45,46] project or the Mass Spectrometer and ground-based Incoherent Scatter model [47,48]. We calculate the temperature profiles from the RDTL signals following the established techniques that have been previously employed at LRL-PFRR [31]. We initially make no correction for pulse pile-up, electronic gating, or signal amplitude. The retrieved temperature profiles for each of the receiver channels are plotted in Figure 3.

There are significant differences in the temperatures derived from the three channels. The differences are greater than the uncertainties due to photon counting. While all the temperature profiles show similar local maxima and minima, with a stratopause at 53 km, the temperatures retrieved from Channel 2 and Channel 3 have higher values than those retrieved from Channel 1 by up to 8 K. These temperature differences are consistent with the differences in the density profiles. The vertical gradient in the Channel 2 and Channel 3

density profiles is less than the gradient in the Channel 1 density profile. This is consistent with a warm bias in Channel 2 and Channel 3.

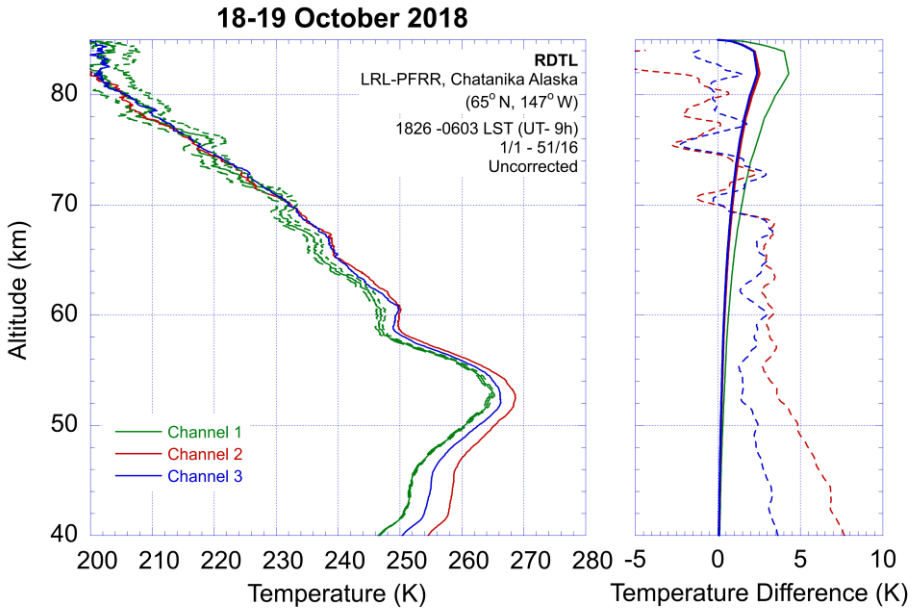

Figure 3. (**Left**) The PFRR-RDTL temperature profiles for Channel 1 ($T_1(z)$), Channel 2 ($T_2(z)$) and Channel 3 ($T_3(z)$) on 18–19 October 2018. (**Right**) The difference between Channel 2 and Channel 3 temperature retrievals relative to the Channel l retrieval ($T_2(z) - T_1(z)$, red-dashed; $T_3(z) - T_1(z)$, blue-dashed; smoothed at 2 km) and signal uncertainties due to photon counting (Channel 1, green-solid; Channel 2, red-solid; Channel 3, blue-solid).

Given that distortion is the greatest at the lower altitudes, we consider three sources of distortion in the signals. These are (i) pulse pile-up, where the MCS will undercount pulses that arrive too close in time to be discriminated, (ii) variation in the detector gain due to the gain switching of the PMT, and (iii) variations in the detector gain due to the amplitude of the signal.

4.2. Correction for Pulse Pile-Up

The lidar photon counting signals are statistical and behave as Poisson random variables (e.g., [38,49]). The PMT pulses have a finite width of 8 ns, so that if a second pulse arrives within 8 ns of the first pulse, the MCS will not detect it as a separate pulse, the pulses have "piled up", and the MCS will undercount the signal. The value of 9 ns is derived from the manufacturer's specifications or experimental characterization. For the Rayleigh lidar, which is a non-paralyzable system, the detector is unresponsive to incoming pulses for a time interval τ_d after a pulse arrives. If a pulse arrives during that interval, τ_d, the pulse is ignored, but the interval is not extended. Thus, a pulse arriving τ_d after an initial pulse is detected regardless of whether any pulses arrive in the intervening τ_d. Thus, the non-paralyzable detector cannot be paralyzed by succeeding pulses. The observed counting rate for a non-paralyzable system, C_{OBS}, is given in terms of the true count rate, C_{TRUE}, as follows:

$$C_{OBS} = C_{TRUE}/(1 + x_{TRUE}) \quad (1)$$

where $x_{TRUE} = C_{TRUE} \times \tau_d$. Solving for C_{TRUE} in terms of C_{OBS}

$$C_{TRUE} = C_{OBS}/(1 + x_{OBS}) \quad (2)$$

where $x_{OBS} = C_{OBS} \times \tau_d$. To correct the pulse pile-up in the three-channel Rayleigh lidar, the data is integrated in 15 min intervals and smoothed over 2 km (~42 range bins) in altitude to increase statistical confidence in the data. The observed count rate is determined by the total signal over 15 min as follows:

$$C_{OBS} = N_{OBS} / \left((\Delta t \times R_L) \left(\frac{2\Delta z}{c} \right) \right) \quad (3)$$

where N_{OBS} is the total lidar signal (including signal, background, and dark signals), R_L is the pulse repetition rate (=20 pps), Δt (=900 s) and Δz (=48 m) are the temporal and spatial resolution of the signal, and c is the speed of light. The count rate is determined on a per-laser-pulse basis, $N_{TOT}/((2\Delta z/c) \times (\Delta t \times R_L))$, where N_{TOT} is the total signal per laser pulse, $2\Delta z/c$ is the time interval corresponding to an individual range bin, and $\Delta t \times R_L$ is the total number of laser pulses. The correction is then applied to the lidar signal as follows:

$$N_{TRUE} = N_{OBS}/(1 - x_{OBS}) \quad (4)$$

The choice of 15 min provides a short enough interval to track signal variations due to energy changes in the laser and sky transmission, while providing enough signal to provide a statistically robust estimate of C_{OBS}. The ratio of the Channel 2 density to the Channel 1 density increases with increasing altitude. When normalizing the ratio to 1 at 85 km, the ratio increases from 0.88 at 40 km. Similarly, the ratio of the Channel 3 density to the Channel 1 density increases with increasing altitude from 0.94 at 40 km to 1 at 85 km. The temperature profiles and the difference in the temperature profiles are plotted in Figure 4. The difference in the temperature values is now reduced relative to the uncorrected data. At 40 km, the difference between the temperatures retrieved from Channel 1 and Channel 2 decreases from 7.98 K to 6.90 K, and the difference between those from Channel 1 and Channel 3 decreases from 3.77 K to 2.30 K. The amount of correction decreases with altitude as the effect of pulse pile-up decreases with the signal levels as they decrease with altitude. However, the differences between the signals in each channel remain greater than the signal uncertainties due to the photon counting statistics. The multi-channel lidars experience issues with alignment between emission and reception between the different channels, an effect that competes with pulse pile-up. The alignment of the multi-channel detection system is optimized on a nightly basis prior to the data acquisition to ensure a consistent overlap between the transmitted beam and the receiver field of view across all channels. This procedure minimizes the channel-to-channel alignment differences.

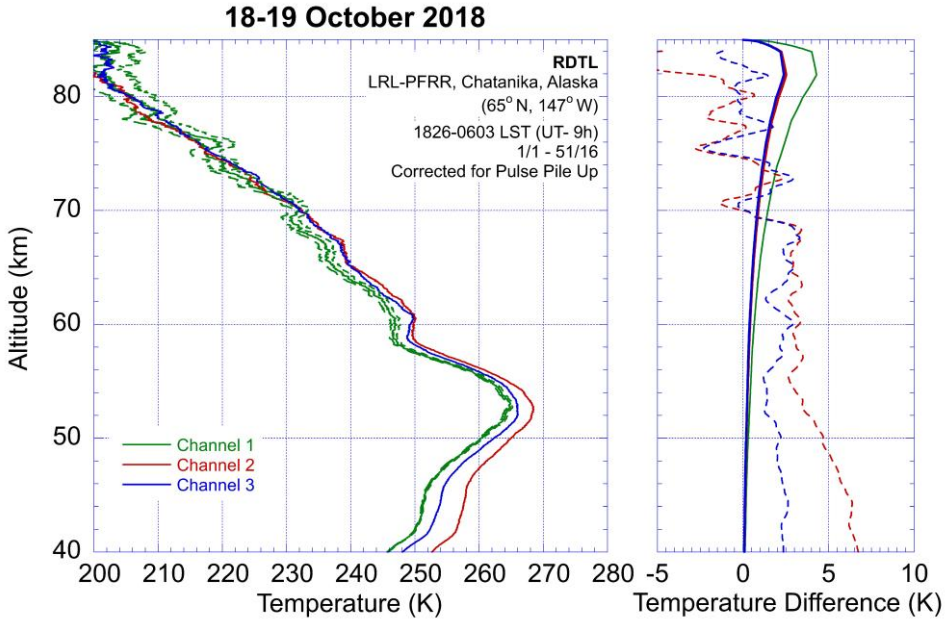

Figure 4. (**Left**) The PFRR-RDTL temperature profiles for Channels 1 ($T_1(z)$), Channel 2 ($T_2(z)$) and Channel 3 ($T_3(z)$) on 18–19 October 2018 corrected for pulse pile-up. (**Right**) The difference between Channel 2 and Channel 3 temperature retrievals relative to the Channel l retrieval ($T_2(z) - T_1(z)$, red-dashed; $T_3(z) - T_1(z)$, blue-dashed; smoothed at 2 km) and signal uncertainties due to photon counting (Channel 1, green-solid; Channel 2, red-solid; Channel 3, blue-solid).

4.3. Detector Gain Switching

The RDTL gain switches the PMTs by controlling the voltage between the photocathode and the first dynode of the PMT. The photocathode is at a voltage of −2000 V, and the anode is at 0 V. A voltage of 200 V is applied to the first dynode of the PMT to reduce the voltage between the photocathode and the first dynode, and thus reduce the acceleration of electrons through the PMT and the gain of the PMT. The application of the 200 V signal is triggered by the laser Q-switch, so that the gain switching commences just before the laser pulse is transmitted. The return signals from the altitudes below a selected altitude are thus detected at low gain, while higher-altitude signals are detected at a high gain.

To determine the variations in the gain following the gain switching, the lidar receiver system was exposed to different intensities of light using light sources that were placed in the telescope. The data acquisition system was triggered with a signal generator. The tests enabled us to determine the effects of the gain switching. The constant light signal mimics a skylight signal that appears constant with altitude. Figure 5 shows the Channel 1 signal with altitude. Ideally, we would expect the signal, $N_g(z)$, to have a constant value, N_0, for $z > z_0$. However, we find that the three channels each have an exponential variation in signal that can be expressed in the following form:

$$N_g(z) = A + B\left(1 - e^{-(z-z_0)/\lambda}\right) \text{ for } z > z_0. \quad (5)$$

The form of the signal is the same as that of an RC time constant in the charging of an RC circuit and reflects the fact that the signal variation is due to the output impedance of the high voltage power supply for the PMT. The coefficients, A, B and λ, are channel-specific constants, and z_o is the corresponding switching altitude. The gain of the PMT is now calculated as follows:

$$g(z) = N_g(z)/N_0. \text{ for } z > z_0 \quad (6)$$

where g(z) = 1 as z $\longrightarrow \infty$. Thus g(z) can be written as, $g(z) = N_g(z)/N_0$. for $z > z_0$ or

$$g(z) = \tilde{A} + \tilde{B}\left(1 - e^{-\frac{(z-z_0)}{\lambda}}\right) \text{ for } z > z_0 \quad (7)$$

where $\tilde{A} = (A/(A + B)$ and $\tilde{B} = (B/(A + B)$. We can now correct the lidar signals for PMT gain switching by dividing the signals that have been corrected for pulse pile-up by g(z). The value of the fitted constants and z_0 for the three channels is listed in Table 3.

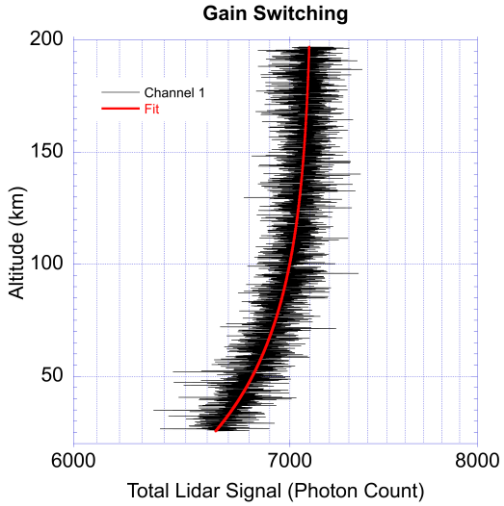

Figure 5. The PFRR_RDTL Channel 1 lidar signal plotted with altitude for the constant light source test on 3 April 2022. The red curve is the curve fitted to the lidar signal.

Table 3. The gain switching fit parameters for the three-channel RDTL.

Parameter	Channel 1	Channel 2	Channel 3
$\tilde{A}$	0.93679	0.95335	0.92570
$\tilde{B}$	0.063210	0.046649	0.074303
λ (km)	58	38	49
z_0 (km)	25.49	32.25	32.30

The ratio of the Channel 2 density to the Channel 1 density increases again with increasing altitude. When normalizing the ratio to 1 at 85 km, the ratio increases from 0.90 at 40 km. Similarly, the ratio of the Channel 3 density to the Channel 1 density increases with increasing altitude from 0.96 at 40 km to 1 at 85 km. The change in the ratio over 45 km has decreased. The differences in the temperature profiles also decrease (Figure 6). At 40 km, the difference between the temperatures retrieved from Channel 1 and Channel 2 decreases from 6.90 K to 6.60 K, and the difference between those from Channel 1 and Channel 3 decreases from 2.30 K to 1.53 K. The amount of correction decreases with altitude as the value of g(z) approaches 1.

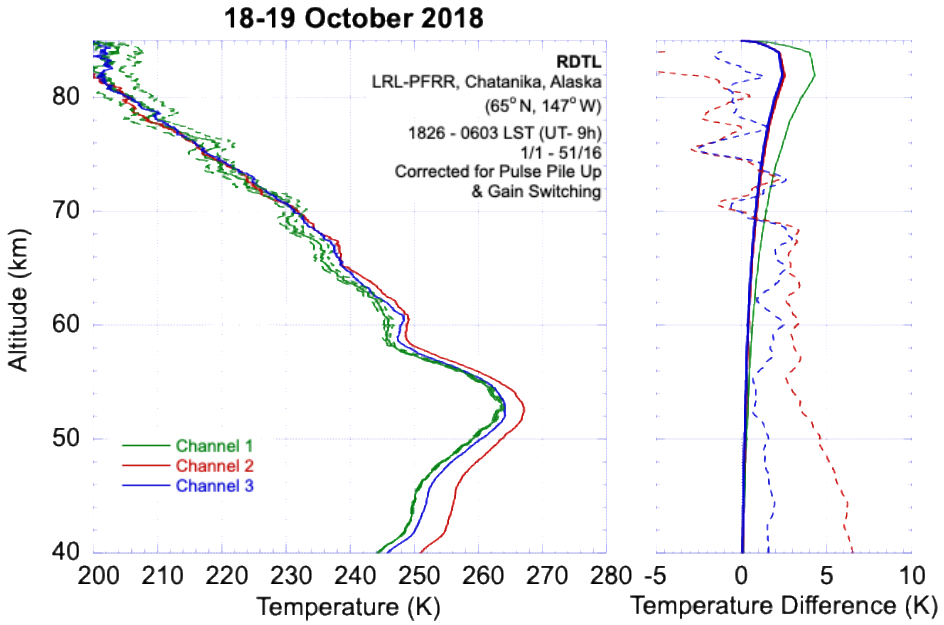

Figure 6. (**Left**) The temperature profile plotted as a function of altitude, measured by the PFRR-RDTL on 18–19 October 2018 after correction for pulse pile-up and PMT gain switching. (**Right**) The difference between Channel 2 and Channel 3 temperature retrievals relative to the Channel l retrieval ($T_2(z) - T_1(z)$, red-dashed; $T_3(z) - T_1(z)$, blue-dashed; smoothed at 2 km) and signal uncertainties due to photon counting (Channel 1, green-solid; Channel 2, red-solid; Channel 3, blue-solid).

4.4. Signal Amplitude

The final correction assumes that the shape of the Channel 1 signal reproduces the atmospheric density profile most faithfully. This is because the Channel 1 signals have the lowest amplitude and, therefore, are the least susceptible to changes in the PMT gain due to variations in the power supply terminal voltage. Thus, the Channel 1 signal is taken as the reference for the Channel 2 and Channel 3 signals. The correction is implemented as a ratio correction.

The temperature and density profiles are first calculated for each of the channels. The temperature profiles from Channel 2 and Channel 3 are compared with those of Channel 1. Starting at the top of the profiles, the profiles are compared moving downward until the altitude where the difference between the temperatures becomes greater than the uncertainties in the difference between the profiles, as follows:

$$(T_1(z) - T_{2,3}(z))^2 > (\Delta T_1(z))^2 + (\Delta T_{2,3}(z))^2 \text{ for } z < z_{S2,3} \quad (8)$$

where ΔT_i is the statistical uncertainty in the temperature moving upward from the bottom of the profiles to the altitude where the difference between the temperatures becomes less than the uncertainties in the difference between the profiles, as follows:

$$(T_1(z) - T_{2,3}(z))^2 < (\Delta T_1(z))^2 + (\Delta T_{2,3}(z))^2 \text{ for } z > z_{S2,3} \quad (9)$$

Once $z_{S2,3}$ is calculated, we now take the ratio of the Channel 1 density profile to the Channel 2 and Channel 3 density profiles. This ratio is calculated as follows:

$$R_{2,3}(z) = \frac{\rho_1(z)}{\rho_1(z_{S2,3})} \times \frac{\rho_{2,3}(zS2,3)}{\rho_{2,3}(z)} \text{ for } z < z_{S2,3} \quad (10)$$

$$R_{2,3}(z) = 1 \text{ for } z > z_{S2,3} \quad (11)$$

The temperatures and uncertainty in temperatures are first calculated for the individual channels from a selected altitude range (e.g., 38 to 85 km) after correcting the total signal for pulse pile-up and blanking response. The individual channel temperatures are then smoothed, and a difference is taken between Channel 1 and the channel for which the factor is being calculated (e.g., Channel 2 or Channel 3). A reference altitude is then calculated where the temperature difference between the two channels is still greater than the total error from the two channels. This altitude is $z_{S1,2}$, and the temperatures are similar between the two compared channels above this altitude.

The ratios between Channel 1 and Channel 3 are also calculated in the same way up to $z_{s1,3}$. For 18 October 2018, the values of z_s for channels 2 and 3 are 69.3 km and 69.1 km, respectively. Figure 7 shows the ratio correction curve for Channel 2 on 18 October 2018. The background signal is removed, and the lidar signal count is then corrected for the ratio correction using,

$$N_{S2}(z) = N_{S2}(z) \times R_{1,2}(z) \quad (12)$$

$$N_{S3}(z) = N_{S3}(z) \times R_{1,3}(z) \quad (13)$$

where N_S is the atmospheric signal component. The background skylight count is then calculated for the individual channels and is added back to the signal. The corrected signal with background noise is then used to calculate the density and temperature profiles.

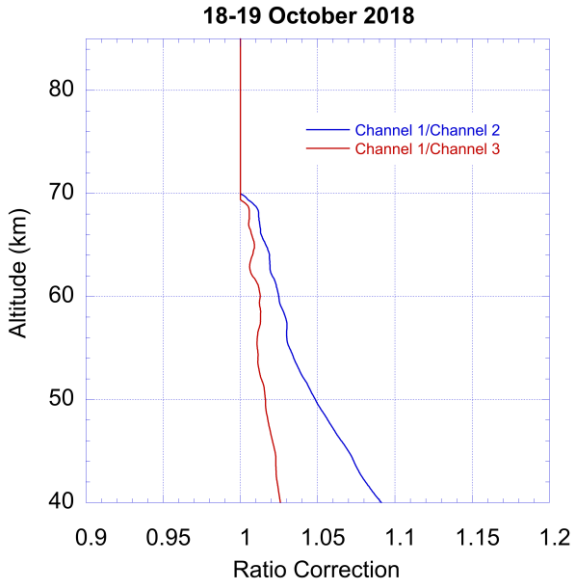

Figure 7. The signal amplitude correction for the PFRR_RDTL channels 2 (ratio Channel 1 to Channel 2) and 3 (ratio Channel 1 to Channel 3) plotted as a function of altitude.

The ratio of the Channel 2 density to the Channel 1 density again increases with increasing altitude. When normalizing the ratio to 1 at 85 km, the ratio increases from 0.97 at 40 km. Similarly, the ratio of the Channel 3 density to the Channel 1 density increases with altitude from 0.98 at 40 km to 1 at 85 km. Figure 8 shows the temperature profiles with altitude for each channel after the corrections for pulse pile-up, blanking response, and ratio are applied to the data. The temperature profiles from the three channels are in good agreement with each other over the whole altitude range. The deviation in temperatures between the three channels is less than 0.05% in all altitudes. As the noise increases above 70 km, the difference in the temperature measurements between the three channels increases. The differences in the temperatures are greater than the uncertainty in the lidar signals above 55 km.

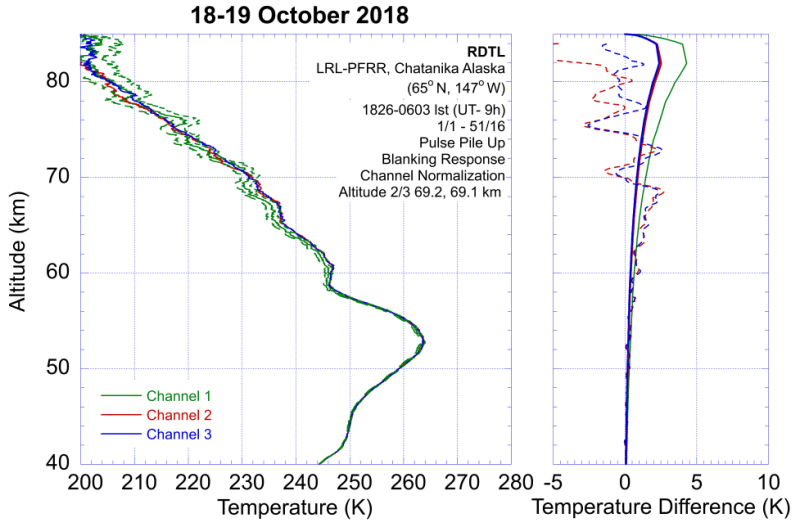

Figure 8. (**Left**) The temperature profile plotted as a function of altitude, measured by the PFRR-RDTL on 18–19 October 2018 after correction for pulse pile-up, blanking response, and signal amplitude correction. (**Right**) The difference between Channel 2 and Channel 3 temperature retrievals relative to the Channel l retrieval ($T_2(z) - T_1(z)$, red-dashed; $T_3(z) - T_1(z)$, blue-dashed; smoothed at 2 km) and signal uncertainties due to photon counting (Channel 1, green-solid; Channel 2, red-solid; Channel 3, blue-solid).

Table 4 summarizes the results of the temperature retrievals for each of the channels as the various corrections are applied. As expected, the corrections are more significant at the lower altitudes with changes of 2.1 K, 10.2 K, and 6.1 K at 40 km and 0.8 K, 3.3 K, and 2.9 K at 60 K for Channel 1, Channel 2, and Channel 3, respectively. The temperatures of the three channels converge to within 0.2 K at 40 km and 0.4 K at 60 km after all the corrections are applied.

Table 4. RDTL temperatures for each channel at selected altitudes.

Correction	**Temperature**				
	40 km	**45 km**	**50 km**	**55 km**	**60 km**
No Correction					
Channel 1	246.6 K	251.8 K	260.5 K	261.5 K	246.9 K
Channel 2	254.6 K	258.7 K	265.3 K	264.5 K	249.8 K
Channel 3	250.4 K	255.1 K	262.7 K	262.9 K	249.4 K
Pulse Pile-Up					
Channel 1	245.8 K	251.5 K	260.4 K	261.4 K	246.9 K
Channel 2	252.7 K	257.9 K	264.9 K	264.4 K	249.8 K
Channel 3	248.1 K	254.2 K	262.3 K	262.8 K	249.3 K
Pulse Pile-Up and Gain Switching					
Channel 1	244.5 K	250.1 K	259.1 K	260.4 K	246.1 K
Channel 2	251.0 K	256.5 K	263.6 K	263.3 K	248.9 K
Channel 3	245.9 K	252.1 K	260.4 K	261.1 K	248.0 K
Pulse Pile-Up, Gain Switching, and Signal Amplitude					
Channel 1	244.5 K	250.1 K	259.1 K	260.4 K	246.1 K
Channel 2	244.4 K	250.4 K	259.1 K	260.7 K	246.5 K
Channel 3	244.3 K	250.3 K	259.2 K	260.7 K	246.5 K

4.5. Combined Three-Channel Temperature Profile

While we have investigated the response of each of the RDTL channels to each of the correction factors, the ultimate goal is to combine the corrected signals in the three channels to yield a single density (Figure 9) and temperature profile (Figure 10) with an associated decrease in temperature. This bias is consistent with the change in density profiles, where the uncorrected density profile has a larger scale height than the corrected density profile. Table 5 summarizes the results of the temperature retrievals for each of the channels as the various corrections are applied. As expected, the corrections are more significant at the lower altitudes with changes of 7.1 K at 40 km and 2.7 at 60 K. The combined corrected temperatures presented in Table 5 agree with the individually corrected temperatures in Table 4 to within 0.2 K or less. The corrected combined temperatures are closest to the corrected Channel 3 temperatures, as the signal in Channel 3 is the largest.

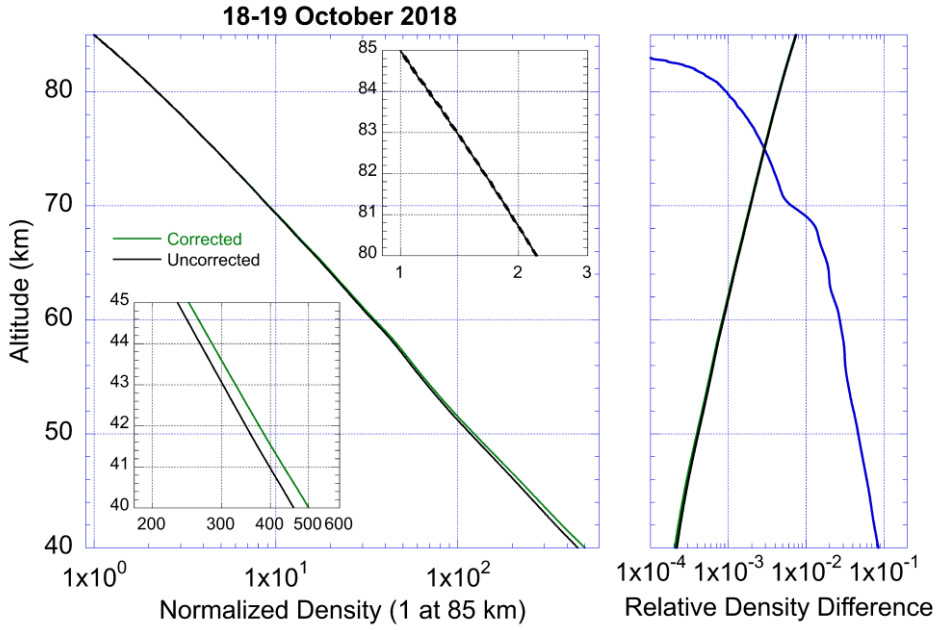

Figure 9. (**Left**) The atmospheric density profile plotted with statistical uncertainties as a function of altitude. The profile is based on the three channels of PFRR-RDTL combined on 18–19 October 2018. The profile is normalized to one at 85 km. The density derived from the uncorrected lidar signal is plotted in black, and the corrected lidar signal is plotted in green. The profiles at 40–45 km and 80–85 km are highlighted as inserts. (**Right**) The relative difference between the corrected and uncorrected density profile (blue) and the expected statistical uncertainty in the corrected profile (black, green).

Table 5. The RDTL temperatures for the combined channels at selected altitudes.

	Temperature (K)				
	40 km	**45 km**	**50 km**	**55 km**	**60 km**
Uncorrected	251.4 K	255.9 K	263.3 K	263.2 K	249.2 K
Corrected	244.3 K	250.4 K	259.2 K	260.5 K	246.5 K
Difference	7.1 K	5.5 K	4.1 K	2.7 K	2.7 K

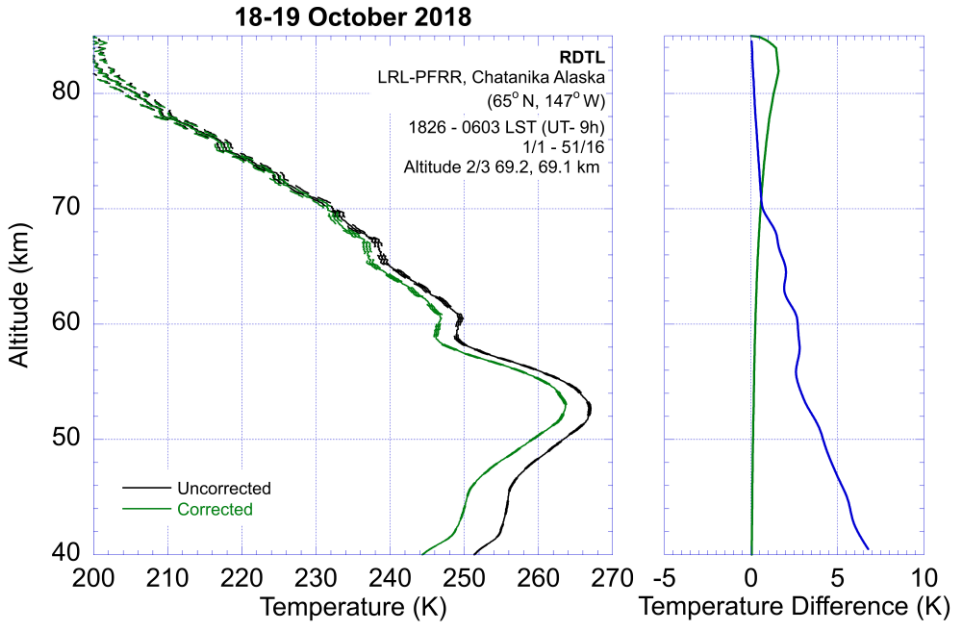

Figure 10. (**Left**) The temperature profile plotted with statistical uncertainties as a function of altitude. The profile is based on the three channels of PFRR-RDTL combined on 18–19 October 2018. (**Right**) The difference between the corrected and uncorrected density profile and the expected statistical uncertainty in the corrected profile (green).

5. Comparison of RDTL Temperatures with MERRA-2 Reanalysis

A comparison of the RDTL temperatures with the Modern-Era Retrospective Analysis for Research and Applications 2 (MERRA-2) reanalysis is shown in Figure 11. The temperature measurements of the Rayleigh lidar extend over 87 nights of observation from September 2018 to April 2022. The RDTL measurements take place under clear sky conditions. The highest number of observations was made in January (17), and the lowest number of observations was made in October (6). The low number of observations in October reflects the low number of clear nights that occurred in that month. The lidar cannot take temperature measurements from May to July due to the lack of nighttime and high background signals during these months. The daily measurements lasted between 3 and 16 h for a total of 832 h. The average observation period lasted 9.5 h. The stratosphere is warm in the months of March, April, August and September, and the temperature increases to over 260 K during this time. A pronounced cycle in the temperature can be observed with a maximum in August and a minimum in January. The months of May, June and July are not included as no lidar measurements were made in these months. The lidar temperatures show the same seasonal trend as the MERRA-2 reanalysis. However, the lidar data shows that late fall and winter conditions are warmer than expected from MERRA. Similar differences between the Rayleigh lidar site observations and the European Centre for Medium-Range Weather Forecasts (ECMWF) have been reported from studies at Andøya, Norway (69° N, 14° E) [50]. In the Andøya study, the measured wintertime middle atmosphere is warmer than that reported by the reanalysis. This is attributed to the fact that gravity waves are not resolved but parameterized in MERRA-2 and that the model has a top lid of 0.01 hPa (~80 km) with a sponge layer beginning at 0.24 hPa (~60 km) [51–53].

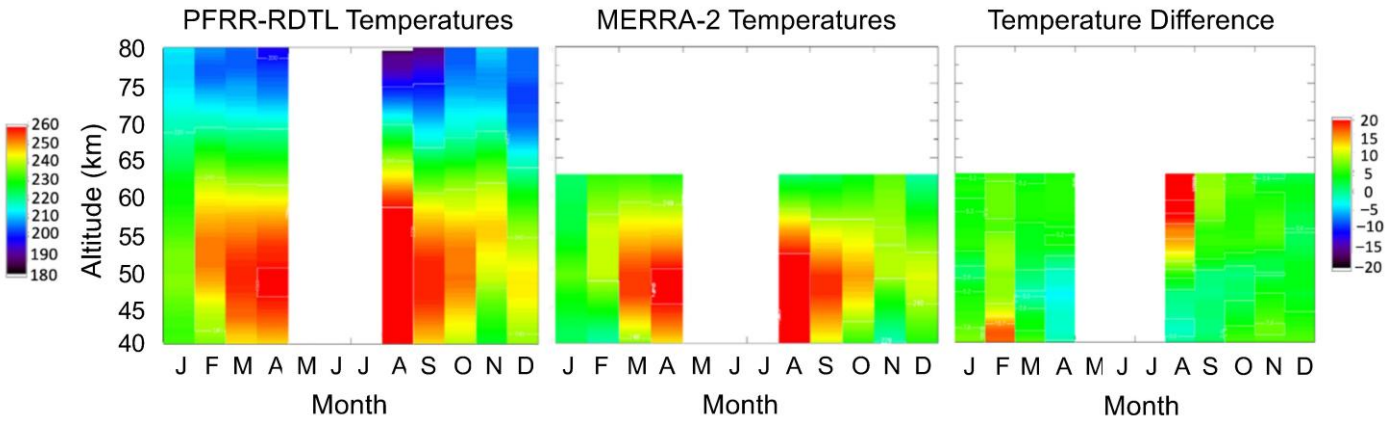

Figure 11. A color plot of the monthly averaged temperature as a function of month and altitude at PFRR, Chatanika, Alaska (65° N, 147° W). (**Left**) The PFRR-RDTL measurements, (**Middle**) the MERRA-2 reanalysis, and (**Right**) the temperature differences between the PFRR-RDTL and MERRA-2. No lidar measurements are made in May, June, and July. The MERRA-2 data are limited to altitudes below 63 km.

6. Conclusions

A single-channel RDTL has been upgraded to a three-channel system. The temperature measurements from the individual channels showed differences in temperatures that were larger than the statistical uncertainties in the values. These differences were largest at the lowest altitudes and decreased with altitude. The differences were consistent with the effects of pulse pile-up, gain switching, and signal amplitude. These three effects contribute to a bias in the density profile where the density is increasingly underestimated as the altitude decreases and appears to have a larger scale height. Under the hydrostatic approximation-based retrieval, this resulted in an overestimate of the temperature. We found the following:

(1) The correction for pulse pile-up results in a decrease of 0.8 K, 1.9 K, and 2.3 K at 40 km in channels 1, 2, and 3, respectively, decreasing to 0.0 K, 0.0 K, and 0.1 K at 60 km.
(2) The combined correction for pulse pile-up and gain switching results in a decrease of 2.1 K, 3.6 K, and 4.5 K in channels 1, 2, and 3, respectively, decreasing to 0.8 K, 0.9 K, and 1.4 K at 60 km.
(3) The combined correction for pulse pile-up, gain switching yields, and signal amplitude results in a decrease of 2.1 K, 10.2 K, and 6.1 K in channels 1, 2, and 3, respectively, decreasing to 0.8 K, 3.3 K, and 2.9 K at 60 km.
(4) The combined correction for pulse pile-up, gain switching yields, and signal amplitude to the combined signal results in a decrease of 7.1 K at 40 km and 2.7 K at 60 km.

We have implemented a scheme to correct the signals in a three-channel Rayleigh lidar system. A comparison of the lidar measurements over three-and-a-half years with MERRA-2 shows differences similar to those observed in a comparison of Rayleigh lidar measurements at Andøya and MERRA-2 [50]. While we have presented our technique in terms of Rayleigh lidar systems, the techniques are also relevant to multi-wavelength aerosol, Raman, and resonance lidar systems, where the ratios of signals from the different channels are used to calculate aerosol properties, water vapor, temperature and wind [54–56].

Author Contributions: Conceptualization, R.C.; methodology, R.C. and S.D.; software, R.C. and S.D.; validation, S.D., R.C. and J.L.; formal analysis, S.D.; investigation, R.C., S.D. and J.L.; resources, R.C., S.D. and J.L.; data curation, S.D. and J.L.; writing—original draft preparation, S.D.; writing—review and editing, S.D. and R.C.; visualization, R.C. and S.D.; supervision, R.C.; project administration,

R.C. and J.L.; funding acquisition, R.C. All authors have read and agreed to the published version of the manuscript.

Funding: This study was supported by the United States National Science Foundation (NSF) and the National Aeronautics and Space Administration (NASA) under the following grants and contracts: NASA 80NSSC21K000, NSF 1651463, NSF 1829161, and NSF 2048628.

Institutional Review Board Statement: Not applicable.

Informed Consent Statement: Not applicable.

Data Availability Statement: The original data presented in the study are openly available in [Three-Channel Rayleigh Lidar System Signal Retrievals] at https://data.mendeley.com/datasets/fsmcntshw3/1 (accessed on 5 February 2026).

Acknowledgments: The authors thank Jennifer Alspach for her assistance with the lidar observations, Biff Williams for helpful discussions, and the staff at Poker Flat Research Range for their ongoing support of lidar operations at the range.

Conflicts of Interest: The funders had no role in the design of the study; in the collection, analyses, or interpretation of data; in the writing of the manuscript; or in the decision to publish the results.

References

1. National Research Council. *Climate Change Science: An Analysis of Some Key Questions*; The National Academies Press: Washington, DC, USA, 2001. [CrossRef]
2. Beig, G.; Keckhut, P.; Lowe, R.P.; Roble, R.G.; Mlynczak, M.G.; Scheer, J.; Fomichev, V.I.; Offermann, D.; French, W.J.R.; Shepherd, M.G.; et al. Review of mesospheric temperature trends. *Rev. Geophys.* **2003**, *41*, 1015. [CrossRef]
3. Beig, G. Long-term trends in the temperature of the mesosphere/lower thermosphere region: 1. Anthropogenic influences. *J. Geophys. Res. Atmos.* **2011**, *116*, A00H11. [CrossRef]
4. Da Costo Louro, P.; Keckhut, P.; Hauchecorne, A.; Wing, R.; Baumgarten, G.; Gerding, M.; Leblanc, T.; Kaifler, B.; Kaifler, N.; Steinbrecht, W.; et al. Decadal variability in mid-atmosphere temperature derived from continuous lidar observations. *J. Atmos. Sol.-Terr. Phys.* **2026**, *280*, 106760. [CrossRef]
5. Hauchecorne, A.; Chanin, M.-L.; Keckhut, P. Climatology and trends of the middle atmospheric temperature (33–87 km) as seen by Rayleigh lidar over the south of France. *J. Geophys. Res.* **1991**, *96*, 15297–15309. [CrossRef]
6. Keckhut, P.; Hauchecorne, A.; Chanin, M.L. Midlatitude long-term variability of the middle atmosphere: Trends and cyclic and episodic changes. *J. Geophys. Res.* **1995**, *100*, 18887–18897.
7. Kishore, P.; Venkat Ratnam, M.; Velicogna, I.; Sivakumar, V.; Bencherif, H.; Clemesha, B.R.; Simonich, D.M.; Batista, P.P.; Beig, G. Long-term trends observed in the middle atmosphere temperatures using ground- based LIDARs and satellite borne measurements. *Ann. Geophys.* **2014**, *32*, 301–317. [CrossRef]
8. Li, T.; Leblanc, T.; McDermid, I.S.; Keckhut, P.; Hauchecorne, A.; Dou, X. Middle atmosphere temperature trend and solar cycle revealed by long-term Rayleigh lidar observations. *J. Geophys. Res. Atmos.* **2011**, *116*, D00P05. [CrossRef]
9. Cnossen, I.; Emmert, J.T.; Garcia, R.R.; Elias, A.G.; Mlynczak, M.G.; Zhang, S.-R. A review of global long-term changes in the mesosphere, thermosphere and ionosphere: A starting point for inclusion in (semi-) empirical models. *Adv. Space Res.* **2024**, *74*, 5991–6011. [CrossRef]
10. Synge, E.H. A method of investigating the higher atmosphere. *Lond. Edinb. Dublin Philos. Mag. J. Sci.* **1930**, *9*, 1014–1020. [CrossRef]
11. Hulburt, E.O. Observations of a Searchlight Beam to an Altitude of 28 Kilometers. *J. Opt. Soc. Am.* **1937**, *27*, 377–382. [CrossRef]
12. Elterman, L. A series of stratospheric temperature profiles obtained with the searchlight technique. *J. Geophys. Res.* **1953**, *58*, 519–530. [CrossRef]
13. Bain, W.C.; Sandford, M.C.W. Light scatter from a laser beam at heights above 40 km. *J. Atmos. Terr. Phys.* **1966**, *28*, 543–552. [CrossRef]
14. Kent, G.S.; Wright, R.W.H. A review of laser radar measurements of atmospheric properties. *J. Atmos. Terr. Phys.* **1970**, *32*, 917–943. [CrossRef]
15. McCormick, P.; Silverberg, E.; Poultney, S.; Van Wijk, U.; Alley, C.O.; Bettinger, R.T. Optical Radar Detection of Backscattering from the Upper Atmosphere. *Nature* **1967**, *215*, 1262–1263. [CrossRef]
16. Hauchecorne, A.; Chanin, M.-L. Density and temperature profiles obtained by lidar between 35 and 70 km. *Geophys. Res. Lett.* **1980**, *7*, 565–568. [CrossRef]
17. Hecht, J. *The Laser Guidebook*, 2nd ed.; Tab Books: Blue Ridge Summit, PA, USA, 1992; p. 498.

18. Silfvast, W.T. *Laser Fundamentals*; Cambridge University Press: Cambridge, UK, 1996; p. 521.
19. Gerding, M.; Wing, R.; Franco-Diaz, E.; Baumgarten, G.; Fiedler, J.; Köpnick, T.; Ostermann, R. The Doppler wind, temperature, and aerosol RMR lidar system at Kühlungsborn, Germany—Part 1: Technical specifications and capabilities. *Atmos. Meas. Tech.* **2024**, *17*, 2789–2809. [CrossRef]
20. Kafle, D.N.; Wickwar, V.B.; Herron, J.P.; Price, J. Characteristics of monochromatic gravity waves in the mesosphere observed by Rayleigh lidar above Logan, Utah. *J. Atmos. Sol.-Terr. Phys.* **2024**, *263*, 106329. [CrossRef]
21. Leblanc, T.; Sica, R.J.; van Gijsel, J.A.E.; Haefele, A.; Payen, G.; Liberti, G. Proposed standardized definitions for vertical resolution and uncertainty in the NDACC lidar ozone and temperature algorithms—Part 3: Temperature uncertainty budget. *Atmos. Meas. Tech.* **2016**, *9*, 4079–4101. [CrossRef]
22. Llamedo, P.; Salvador, J.; de la Torre, A.; Quiroga, J.; Alexander, P.; Hierro, R.; Schmidt, T.; Pazmiño, A.; Quel, E. 11 years of Rayleigh lidar observations of gravity wave activity above the southern tip of South America. *J. Geophys. Res. Atmos.* **2019**, *124*, 451–467. [CrossRef]
23. Sharma, S.; Vaishnav, R.; Shukla, K.K.; Lal, S.; Chandra, H.; Acharya, Y.B. Rayleigh Lidar observed atmospheric temperature characteristics over a western Indian location: Intercomparison with satellite observations and models. *Eur. Phys. J. D* **2017**, *71*, 187. [CrossRef]
24. Wing, R.; Hauchecorne, A.; Keckhut, P.; Godin-Beekmann, S.; Khaykin, S.; McCullough, E.M.; Mariscal, J.-F.; d'Almeida, É. Lidar temperature series in the middle atmosphere as a reference data set—Part 1: Improved retrievals and a 20-year cross-validation of two co-located French lidars. *Atmos. Meas. Tech.* **2018**, *11*, 5531–5547. [CrossRef]
25. Zou, X.; Yang, G.; Chen, L.; Wang, J.; Du, L. Rayleigh Lidar Observations and Comparisons with TIMED/SABER of Typical Case Studies in Beijing (40.5° N, 116.2° E), China. *Atmosphere* **2021**, *12*, 1237. [CrossRef]
26. Fiedler, J.; Baumgarten, G. The ALOMAR Rayleigh/Mie/Raman lidar: Status after 30 years of operation. *Atmos. Meas. Tech.* **2024**, *17*, 5841–5859. [CrossRef]
27. Keckhut, P.; Hauchecorne, A.; Chanin, M.-L. A Critical Review of the Database Acquired for the Long-Term Surveillance of the Middle Atmosphere by the French Rayleigh Lidars. *J. Atmos. Ocean. Technol.* **1993**, *10*, 850–867. [CrossRef]
28. von Zahn, U.; von Cossart, G.; Fiedler, J.; Fricke, K.H.; Nelke, G.; Baumgarten, G.; Rees, D.; Hauchecorne, A.; Adolfsen, K. The ALOMAR Rayleigh/Mie/Raman lidar: Objectives, configuration, and performance. *Ann. Geophys.* **2000**, *18*, 815–833. [CrossRef]
29. Mizutani, K.; Itabe, T.; Yasui, M.; Aoki, T.; Murayama, Y.; Collins, R.L. Rayleigh and Rayleigh Doppler Lidars for the Observations of the Arctic Middle Atmosphere. *IEICE Trans. Commun.* **2000**, *E83-B*, 2004–2009.
30. Cutler, L.J.; Collins, R.L.; Mizutani, K.; Itabe, T. Rayleigh lidar observations of mesospheric inversion layers at Poker Flat, Alaska (65° N, 147° W). *Geophys. Res. Lett.* **2001**, *28*, 1467–1470. [CrossRef]
31. Triplett, C.C.; Li, J.; Collins, R.L.; Lehmacher, G.A.; Barjatya, A.; Fritts, D.C.; Strelnikov, B.; Lübken, F.; Thurairajah, B.; Harvey, V.L.; et al. Observations of reduced turbulence and wave activity in the Arctic middle atmosphere following the January 2015 sudden stratospheric warming. *J. Geophys. Res. Atmos.* **2018**, *123*, 13259–13276. [CrossRef]
32. Alspach, J.H. Lidar and Satellite Studies of Noctilucent Clouds Over Alaska. Master's Thesis, University of Alaska, Fairbanks, AK, USA, 2020.
33. Thurairajah, B.; Collins, R.L.; Mizutani, K. Multi-year temperature measurements of the middle atmosphere at Chatanika, Alaska (65° N, 147° W). *Earth Planets Space* **2009**, *61*, 755–764. [CrossRef]
34. Sica, R.J.; Izawa, M.R.M.; Walker, K.A.; Boone, C.; Petelina, S.V.; Argall, P.S.; Bernath, P.; Burns, G.B.; Catoire, V.; Collins, R.L.; et al. Validation of the Atmospheric Chemistry Experiment (ACE) version 2.2 temperature using ground-based and space-borne measurements. *Atmos. Chem. Phys.* **2008**, *8*, 35–62. [CrossRef]
35. Evans, R.D. *The Atomic Nucleus*; McGraw-Hill: New York, NY, USA, 1995; p. 950.
36. Irving, B.K. Rayleigh Lidar Studies of Mesospheric Inversion Layers at Poker Flat Research Range, Chatanika, Alaska. Master's Thesis, University of Alaska, Fairbanks, AK, USA, 2012.
37. Gardner, C.S. Performance capabilities of middle-atmosphere temperature lidars: Comparison of Na, Fe, K, Ca, Ca^+, and Rayleigh systems. *Appl. Opt.* **2004**, *43*, 4941–4956. [CrossRef]
38. Papoulis, A.; Pillai, S.U. *Probability, Random Variables and Stochastic Processes*; Mc Graw Hill: New York, NY, USA, 2002; p. 852.
39. Wang, W. Spectral Estimation of Signal and Noise Power in Rayleigh Lidar Measurements of the Middle Atmosphere. Master's Thesis, University of Alaska, Fairbanks, AK, USA, 2003.
40. Leblanc, T.; McDermid, I.S.; Hauchecorne, A.; Keckhut, P. Evaluation of optimization of lidar temperature analysis algorithms using simulated data. *J. Geophys. Res.* **1998**, *103*, 6177–6187. [CrossRef]
41. Whiteman, D.N.; Melfi, S.H.; Ferrare, R.A. Raman lidar system for the measurement of water vapor and aerosols in the Earth's atmosphere. *Appl. Opt.* **1992**, *31*, 3068–3082. [CrossRef] [PubMed]
42. Stevens, M.H.; Englert, C.R.; DeLand, M.T.; Hervig, M. Polar mesospheric clouds formed from space shuttle exhaust. *Geophys. Res. Lett.* **2003**, *30*, 1546. [CrossRef]

43. Stevens, M.H.; Meier, R.R.; Chu, X.; DeLand, M.T.; Plane, J.M.C. Antarctic mesospheric clouds formed from space shuttle exhaust. *Geophys. Res. Lett.* **2005**, *32*, L13810. [CrossRef]
44. Kelley, M.C.; Nicolls, M.J.; Varney, R.H.; Collins, R.L.; Doe, R.; Plane, J.M.C.; Thayer, J.; Taylor, M.; Thurairajah, B.; Mizutani, K. Radar, lidar, and optical observations in the polar summer mesosphere shortly after a space shuttle launch. *J. Geophys. Res. Space Phys.* **2010**, *115*, A05304. [CrossRef]
45. SPARC. SPARC Intercomparison of Middle Atmosphere Climatologies. In *SPARC Report 3*; APARC: Jülich, Germany, 2002; p. 96.
46. Randel, W.; Udelhofen, P.; Fleming, E.; Geller, M.; Gelman, M.; Hamilton, K.; Karoly, D.; Ortland, D.; Pawson, S.; Swinbank, R.; et al. The SPARC intercomparison of middle-atmosphere climatologies. *J. Clim.* **2004**, *17*, 986–1003. [CrossRef]
47. Hedin, A.E. Extension of the MSIS Thermosphere Model into the middle and lower atmosphere. *J. Geophys. Res.* **1991**, *96*, 1159–1172. [CrossRef]
48. Emmert, J.T.; Drob, D.P.; Picone, J.M.; Siskind, D.E.; Jones, M., Jr.; Mlynczak, M.G.; Bernath, P.F.; Chu, X.; Doornbos, E.; Funke, B.; et al. NRLMSIS 2.0: A whole-atmosphere empirical model of temperature and neutral species densities. *Earth Space Sci.* **2021**, *8*, e2020EA001321. [CrossRef]
49. Taylor, J.C. *An Introduction to Measure and Probability*; Springer: New York, NY, USA, 1996; ISBN 978-0-387-94830-0.
50. Schöch, A.; Baumgarten, G.; Fiedler, J. Polar middle atmosphere temperature climatology from Rayleigh lidar measurements at ALOMAR (69° N). *Ann. Geophys.* **2008**, *26*, 1681–1698. [CrossRef]
51. Molod, A.; Takacs, L.; Suarez, M.; Bacmeister, J. Development of the GEOS-5 atmospheric general circulation model: Evolution from MERRA to MERRA-2. *Geosci. Model Dev.* **2015**, *8*, 1339–1356. [CrossRef]
52. Fujiwara, M.; Wright, J.S.; Manney, G.L.; Gray, L.J.; Anstey, J.; Birner, T.; Davis, S.M.; Gerber, E.P.; Harvey, V.L.; Kim, J.; et al. Introduction to the SPARC Reanalysis Intercomparison Project (S-RIP) and overview of the reanalysis systems. *Atmos. Chem. Phys.* **2017**, *17*, 1417–1452. [CrossRef]
53. Gelaro, R.; McCarty, W.; Suárez, M.J.; Todling, R.; Molod, A.; Takacs, L.; Randles, C.A.; Darmenov, A.; Bosilovich, M.G.; Reichle, R.; et al. The Modern-Era Retrospective Analysis for Research and Applications, Version 2 (MERRA-2). *J. Clim.* **2017**, *30*, 5419–5454. [CrossRef]
54. Ansmann, A.; Müller, D. Lidar and Atmospheric Aerosol Particles. In *Lidar: Range Resolved Atmospheric Remote Sensing of the Atmosphere*; Weitkamp, C., Ed.; Springer: New York, NY, USA, 2005; p. 455.
55. Chu, X.; Papen, G.C. Resonance fluorescence lidar for measurements of the middle and upper atmosphere. In *Laser Remote Sensing*; Fuji, T., Fukuchi, T., Eds.; Taylor & Francis: Boca Raton, FL, USA, 2005; p. 888.
56. Wandinger, U. Raman Lidar. In *Lidar: Range Resolved Atmospheric Remote Sensing of the Atmosphere*; Weitkamp, C., Ed.; Springer: New York, NY, USA, 2005; p. 455.